

Simulations of Observations with the Far-Infrared Surveyor: Design Overview and Current Status

By

Woong-Seob JEONG*, Soojong PAK*, Hyung Mok LEE*, Sam KIM*,
Mikako MATSUURA†§, Takao NAKAGAWA†, Issei YAMAMURA†, Hiroshi MURAKAMI†
Shuji MATSUURA†, Mitsunobu KAWADA†, Hidehiro KANEDA†, and Hiroshi SHIBAI†

(November 1, 2000)

Abstract: The Far-Infrared Surveyor (FIS) is one of the on-board instruments on the ASTRO-F satellite, which will be launched in early 2004. The first a half year of its mission period of 500 days is dedicated to an all sky survey in four bands between 50 and 200 μm . On the basis of the present hardware specifications and configurations of the FIS, we have written a computer program to simulate the FIS. The program can be used to evaluate the performance of the instrument as well as to produce input for the data reduction system. In this paper, we describe the current status of the program. As an example of the usage of the simulation program, we present the expected observing data for three different detector sampling rates. The functions which should be implemented into the program, in the future, are enumerated.

1. INTRODUCTION

The FIS (Far-Infrared Surveyor, Kawada 1998) is one of the focal plane instruments on-board the ASTRO-F (previously known as IRIS, Murakami 1998). The FIS is equipped with two-dimensional arrays and covers four wavelength bands: N60 (50 – 70 μm), WIDE-S (50 – 110 μm), N170 (150 – 200 μm), and WIDE-L (110 – 200 μm) (see Table 1 in Kawada 1998). FIS observes in both survey and pointing observation modes. In the survey mode, the detector pixels will continuously scan the sky while the satellite spins around itself on Sun Synchronous orbit with a 100 minute period.

We have developed a computer simulation software of the FIS survey mode observations. The purpose of our simulation software includes:

* Astronomy Program in Graduate School of Earth and Environmental Sciences, Seoul National University, Shillim-Dong Kwanak-Gu, Seoul 151-742, South Korea; jeongws@astro.snu.ac.kr

† Institute of Space and Astronautical Science, Yoshino-dai 3-1-1, Sagamihara, Kanagawa 229-8510, Japan

‡ Department of Astrophysics, Nagoya University, Furo-cho, Chikusa-ku, Nagoya 464-8602, Japan

§ Department of Astronomy, University of Tokyo, Hongo 7-3-1, Bunkyo-ku, Tokyo 133-0033, Japan

1. To evaluate the hardware design and its performance;
2. To find optimum observing parameter sets while the satellite is in orbit;
3. To provide input data for the reduction software to be completed before launch.

The FISVI is a virtual instrument program written in IDL to achieve the above objectives. In this paper, we present the simulation for the N170 (150 – 200 μm) band. Extension to other FIS bands is left as a future work. N170 band uses a 2×15 array of stressed Ge:Ga detectors. Under current design of the optical system, one detector element covers a $44.2'' \times 44.2''$ square shaped ares in the sky, and the array is tilted against the scanning direction by 26.5° to achieve Nyquist sampling in the cross-scan direction (perpendicular to the scanning direction).

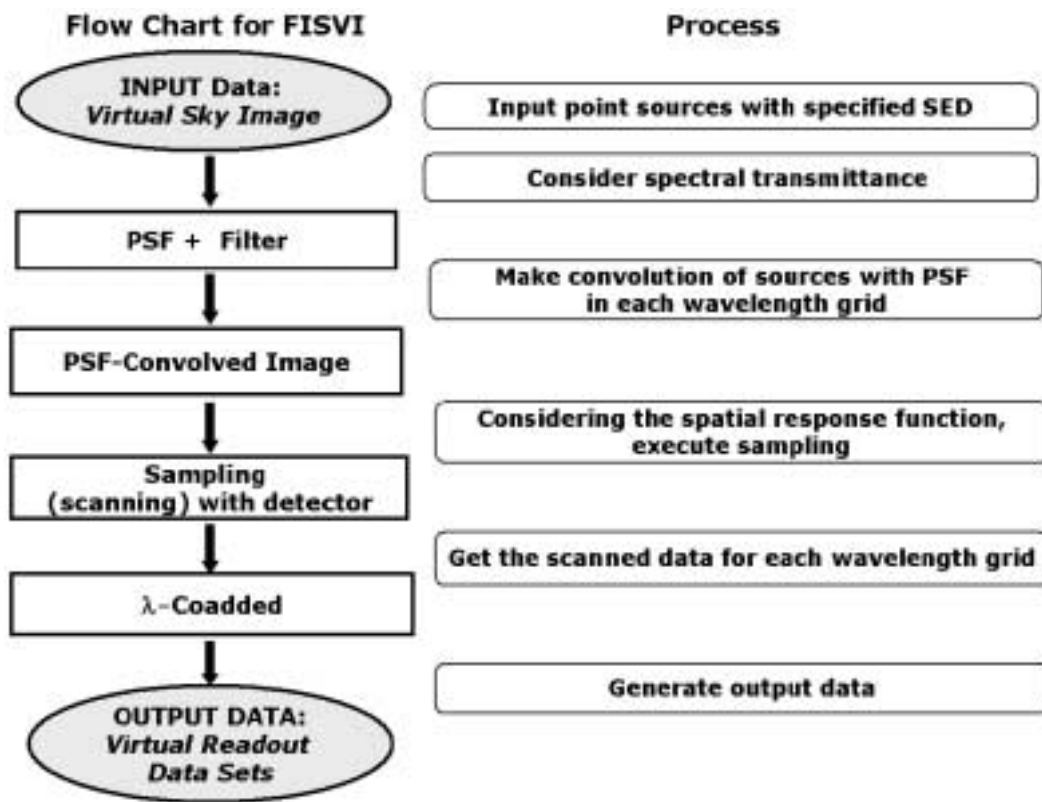


Fig. 1: Structure of software and flow chart of the FIS Virtual Instrument Program (FISVI)

2. THE FIS VIRTUAL INSTRUMENT PROGRAM (FISVI)

2.1 Overview

The first generation of the FIS simulation program is described in Matsuura et al. (in preparation). The program considered the configuration and size of the detector elements, sampling rate, and the telescope optics. In the program, the spatial response function, which takes into account the detector shape and the diffraction pattern of the telescope, is calculated for each

detector element. A detector element is assumed to have square shaped response function. The (virtual) sky is scanned with the convolution of the diffraction pattern and the detector response. For the point spread function (PSF) of the telescope, the program adopts calculated results using ZEMAX optical simulation software including the shadow due to the baffle around the secondary mirror. The transmittance of the filters and the FIS optical elements, as well as the spectral response function of the detector are newly implemented.

We have written the 2nd version of simulator based on the program by Matsuura et al. Instead of scanning the sky by the telescope plus detector convolved PSF, we first perform convolution of a virtual sky with the telescope's PSF and then simulate the scanning of the virtual sky with the detector array. This modification improves the calculation speed significantly.

2.2 Optics and Detector Response

The radiation from the celestial source, $F_\lambda(\alpha, \delta)$, where α , and δ are right ascension and declination, respectively, is projected onto the focal plane at (x, y) . The monochromatic pixel value (energy absorbed by a pixel per unit time per unit wavelength interval), $P_\lambda(x, y)$, can be expressed by convolution of responsivity weighted flux with the PSF at a given λ .

The FIS detectors are not located on optical axis of the focal Plane. In the current version, however, we adopted the PSF at the optical axis. The aberrations due to offset from the center as well as the off-axis optics in the FIS will be considered in future.

The spectra of the input sources are taken into account. We need PSFs at arbitrary wavelengths while the PSF is calculated only at $\lambda = 200\mu\text{m}$. The necessary PSFs at given wavelengths are obtained by linear scaling in λ/λ_0 using the computed PSF at $\lambda_0 = 200\mu\text{m}$.

Transmittance of the FIS optics and the filters are included in the program. Roughly speaking, the sensitivity of the stressed Ge:Ga detector is inversely proportional to the wavelength up to certain cut-off wavelength (e.g. Kazanskii, Richards, & Haller 1977). In the real detector, however, the cut-off is not very sharp and the responsivity drops rather gently from 150 to 200 μm . The measurement by Makiuti et al. (1998) for the responsivity of the detector type to be used for N170 band shows substantial noise mainly due to the difficulties in correcting the filter transmission. Thus we have drawn a smooth curve based on this measurement for our calculation. The result is shown in Fig. 2 as a broken line. The drop toward the long wavelength begins at around 150 μm and the responsivity becomes very small at around 200 μm . The actual spectral response of the detectors for N170 on FIS will be somewhat different from the one we used here because of the uncertainties in the responsivity of the detector, and the curves in Fig. 2 should be considered as tentative. The transmittance of the filter (Takahashi et al. 2000) including the FIS optics is also shown in Fig. 2 as a dotted line, together with the combined responsivity of the filter-detector system as a solid line. Since the detector responsivity is relative value, we normalized the combined responsivity to 1 at the peak value (at around 170 μm). We note that the combined responsivity of the filter-detector system is narrowly peaked at around 170 μm .

2.3 Input Data

The input data shown in Fig. 3 consist of 20 point sources of various fluxes. In the current program, we use arbitrary units for the flux. As for the spectral energy distribution (SED) of the sources, we have examined both flat spectra (i.e., constant F_λ , where $F_\lambda d\lambda$ is the energy flux in $\lambda \sim \lambda + d\lambda$) and Rayleigh-Jeans tail of the black-body spectra (i.e., $F_\lambda \propto \lambda^{-4}$). We

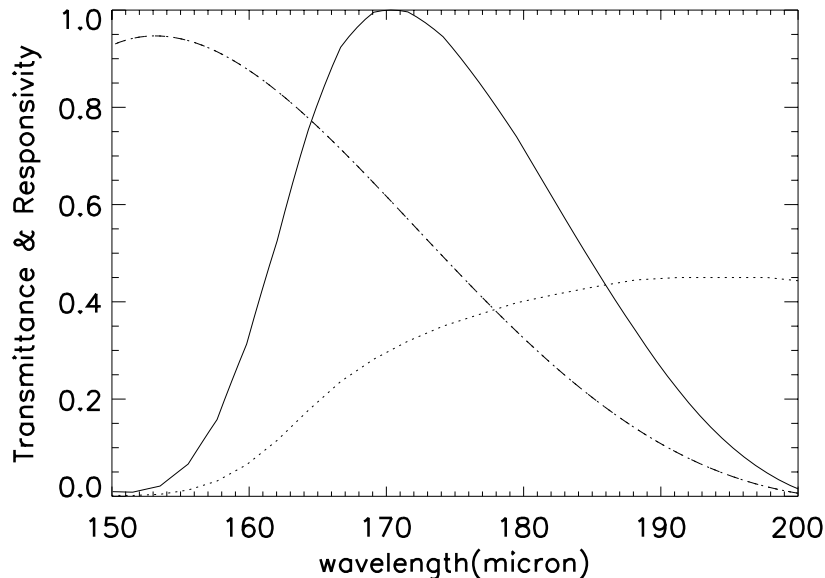


Fig. 2: The transmittance of the filter (including the FIS optics: dotted), the responsivity of the detector (dash dotted), and filter-detector combined responsivity as a function of wavelength (solid). The combined response is normalized such that the peak value becomes 1 (at around $\lambda = 170\mu\text{m}$).

have taken into account the spectral response function of N170, which is shown in Fig. 2, to obtain the final images by adding up monochromatic images at discrete wavelength grids (see §2.4). More realistic SEDs can be accommodated in our program.

2.4 Detector and Readout

The satellite will scan the sky with a speed of $3.6 \text{ arcmin s}^{-1}$ (see Murakami 1998). We can simulate this by moving the detector arrays on the PSF-convolved image. The photon energy is converted to charges and stored in the charge integrating amplifier. In our program, the readout values during two subsequent sampling steps is obtained by integrating $P_\lambda(x, y)$ over the time and over the wavelengths. In order to carry out the time integration, we take the pixel values at discrete times separated by small time-steps ($\Delta t = 1/64 \text{ sec}$) to mimic a continuous motion of the detector. Thus, a readout with 16 Hz sampling rate is a summation of pixel values at four different time-steps. The representative position of one readout is assumed to be a mid-point of two positions: one at the beginning and the other at the end of the integration. The wavelength integration (λ -coaddition process) is performed by dividing the entire band into discrete wavelengths with $\Delta\lambda = 5\mu\text{m}$ interval.

3. RESULTING IMAGES

We have applied our program to a virtual distribution of 20 point sources over $10 \text{ arcmin} \times 10 \text{ arcmin}$ area, as shown in Fig. 3, together with one pixel element as a square shaped box. The scanning direction is indicated as an arrow.

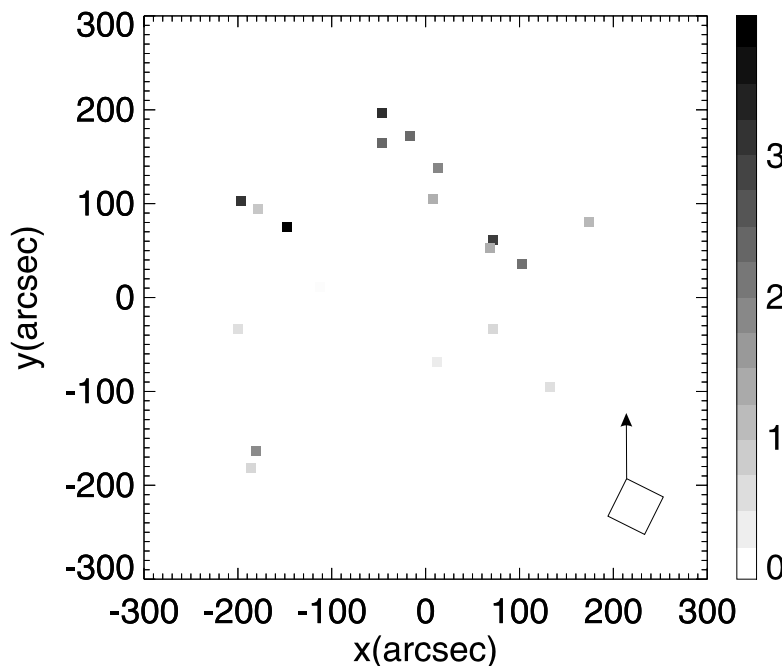


Fig. 3: Virtual input data composed of 20 point sources in the sky. These sources are assumed to have either flat spectra (i.e., constant F_λ) or Rayleigh-Jeans tail of black body spectra (i.e., $F_\lambda \propto \lambda^{-4}$). The numbers shown in the color bar is the flux in arbitrary units. The tilted square box indicates a detector pixel projected on the sky relative to the scanning direction which is shown as an arrow.

In Fig. 4, we have shown the monochromatic images at 150 and 200 μm . Obviously, the image at 150 μm is shaper than that of 200 μm because of the difference in PSF: the diffraction limit at 150 and 200 μm are 53.9'' and 71.9'', respectively. Also notice the extended light well outside the bright sources resulting from the outer tail of the PSF. Such features are most clearly seen around a group of sources at $(x, y) \approx (-40, 180)$ and $(100, 20)$.

Actual images obtained by integrating monochromatic ones over λ are shown in Fig. 5. Here we have assumed that, for each source, the integrated flux from $\lambda = 150$ to 200 μm are the same for flat and Rayleigh-Jeans tail SEDs. We find that these two images are nearly identical. The SED appears to have very little effects on the ‘effective wavelength’, that represents a wavelength of a given band, for N170. This is mainly because of the narrowness of the combined responsivity of the filters and the detector shown in Fig. 2.

4. DISCUSSIONS

Our program can be used to achieve the tasks listed in section 1. However, there are still substantial uncertainties in instrumental characteristics such as the spectral response of the detectors. Also the program is in a preliminary stage and more effects are to be taken into account. In this section, we briefly discuss the effects of sampling rate on the observed data and list the necessary works in the future on this program. In the current version, we assumed that the photon flux instantaneously changes into current.

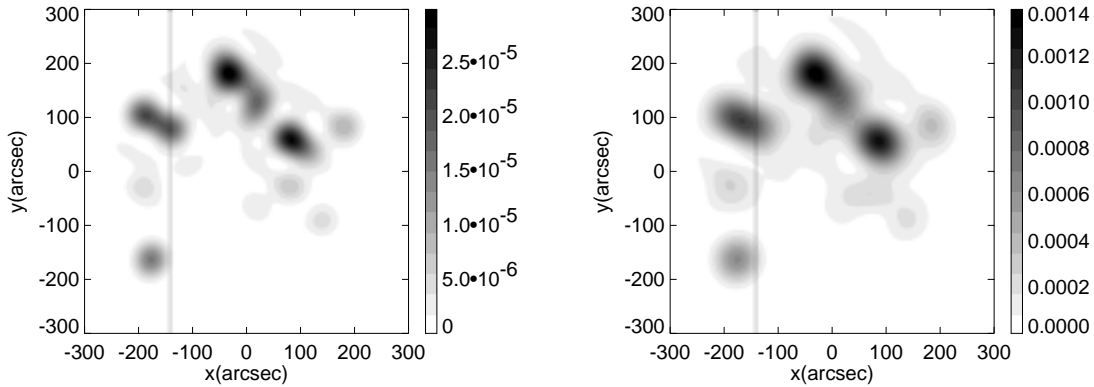


Fig. 4: PSF convolved image (in linear scale in brightness) at $150\ \mu\text{m}$ (left panel) and at $200\ \mu\text{m}$ (right panel) on the focal plane. The vertical lines at $x = -142''$ indicate the cuts where we obtained the one-dimensional profiles shown in Fig. 6. The numbers shown along the color bars are the flux densities in arbitrary units.

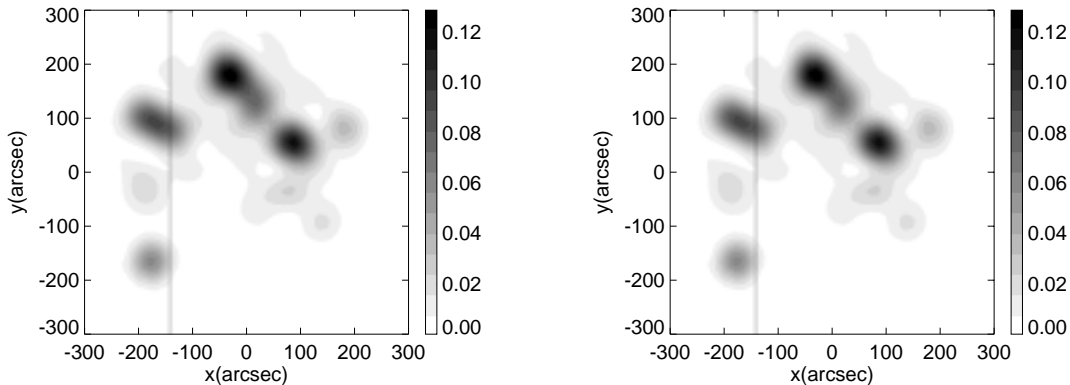


Fig. 5: λ -coadded image for flat SED (left), and Rayleigh-Jeans tail of black body SED (right). Since the throughput spectral response has a rather narrow width, the effective wavelength is not much sensitive to the spectral shape of the source, and these two images are nearly identical. The numbers shown along the color bars are the flux densities in arbitrary units.

4.1 Effects of Sampling Rate

The sampling rate should be chosen to optimize the data quality and the amount of data. We have examined three different sampling rates: the nominal (16 Hz), half of the nominal (8 Hz), and twice the nominal (32 Hz). Fig. 6 shows a result of a scan along $x = -142''$ at two different wavelengths ($\lambda = 150$ and $200\ \mu\text{m}$) in the upper panels. We also show the λ -coadded results for the flat and Rayleigh-Jeans tail SEDs in the lower panels. The low sampling rate generally produces somewhat poorer profiles. Also notice that there are some differences in the one-dimensional profiles between 150 and $200\ \mu\text{m}$ scans. The small peaks at around $y = -40''$ and $200''$ are less pronounced in the $150\ \mu\text{m}$ profiles. These regions do not contain any source, and the diffuse components are mainly due to the tail of the PSF. Since the PSF is narrower

for shorter wavelengths, we see less diffuse light at $150\ \mu\text{m}$ than at $200\ \mu\text{m}$.

The difference between the scanned data with 16 and 32 Hz sampling is clearly much smaller than that between 16 and 8 Hz samplings. Therefore, the current choice of nominal 16 Hz sampling appears to be appropriate for FIS observations for the ideal sky. Sampling rate of 8 Hz give substantially distorted image profiles for bright sources. It may be possible to recover some aspects of the sources from under sampled images using PSF fitting procedure, but it is beyond the scope of this paper to examine such issue.

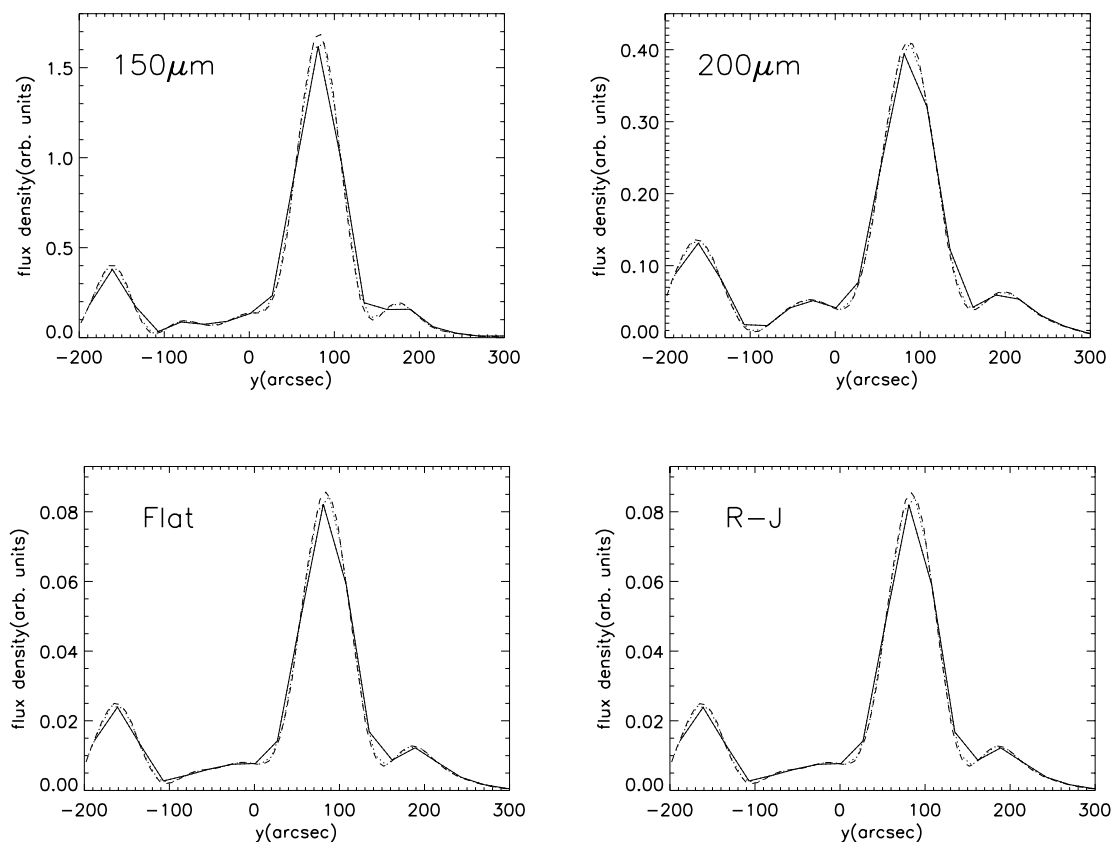


Fig. 6: The brightness distribution along one-dimensional cut shown in Fig. 3 with different sampling rates (8, 16 and 32 Hz) at $150\ \mu\text{m}$ (upper left), and $200\ \mu\text{m}$ (upper right), respectively. The lower panels show the same for λ -coadded scanned data of flat (left) and Rayleigh-Jeans tail of blackbody (right) SEDs, respectively. The solid, dotted, and broken lines represent 8 Hz, 16 Hz, and 32 Hz sampling results, respectively. Clearly 8 Hz sampling gives rather poor information regarding the peak positions and fluxes.

4.2 Future Work

The complex response of the hardware of the FIS has not been fully incorporated in the current version of FISVI. We will embody some more realistic effects in future simulations. For example, spatial response function of the detector is not exactly a box function, especially for unstressed Ge:Ga detector arrays (see Fig. 3 in Hiromoto et al. 1998). The projected shape of

the detector is distorted by optical aberrations. The effect of noise should also be taken into account.

The Ge:Ga detector changes its response depending on the incident photons. Due to the transient response, the detector output versus input flux would be a non-linear function. It also affects the apparent detected position of the sources. Okamura (2000) measured the time constants of the transient effects in the laboratory. To correct the transient response is one of the key issues on the ASTRO-F data reduction, and therefore the future program will include such effects.

The charges from the detector are collected at the charge integrating amplifier. The integrated charges are discharged by resetting every 2 – 5 minutes. Longer discharge intervals are preferred because each reset needs a short pause to settle down. However, the integrating amplifier can be saturated, if the detector sees a bright source. Thus we should find an optimum mode by simulating more realistic sky data and correct values for the optics-detector combined sensitivities.

Finally, the effects of cosmic ray hitting will have to be included in the program. The effects of cosmic ray hitting are: (1) creation of a sharp spike (glitch) and an associated after effect and (2) changes in response of the detector in both short and long time scales. The effects may differ depending on the nature of impacting particle, the energy, and the location of the impact. Proper implementation of these effects into the simulation program will help us to investigate how to detect and correct the spikes and tails, and to optimize the curing method of detector response change after the passage of South-Atlantic Anomaly (SAA) where most of the cosmic ray hitting will take place.

ACKNOWLEDGMENT

This work was financially supported in part by the BK21 Project of the Korean Government, and in part by the KOSEF-JSPS corporative research program. M.M. is supported by the research fellowship of JSPS for the Young Scientists.

REFERENCES

- Hiromoto, N., Fujiwara, M., Shibai, H., Hirao, T., Nakagawa, T., & Kawada, M. 1998, SPIE Proc., 3354, 48
- Kawada, M. 1998, SPIE Proc., 3354, 905
- Kazanskii, A. G., Richards, P. L., & Haller, E. E. 1977, Appl. Phys. Lett., 31, 496
- Makiuti, S., Doi, Y., Shibai, H., Hiromoto, N., Nakagawa, T., Kawada, M., Okumura, K., & Okuda, H. 1998, SPIE Proc., 3354, 261
- Murakami, H., 1998, SPIE Proc., 3356, 471
- Okamura, Y. 2000, Master Thesis, University of Tokyo
- Takahashi, H. et al. 2000, SPIE Proc., 4013, 47